

Role of Halides in the Ordered Structure Transitions of Heated Gold Nanocrystal Superlattices

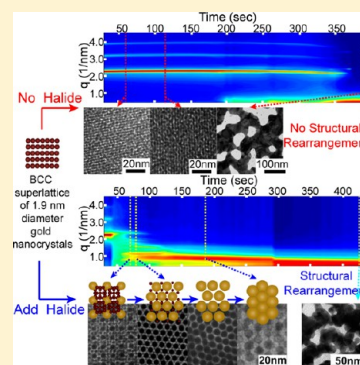
Yixuan Yu,[†] Brian W. Goodfellow,[†] Michael R. Rasch,[†] Christian Bosoy,[†] Detlef-M. Smilgies,[‡] and Brian A. Korgel^{*,†}

[†]McKetta Department of Chemical Engineering, Texas Materials Institute and Center for Nano- and Molecular Science and Technology, The University of Texas at Austin, Austin, Texas 78712-1062, United States

[‡]Cornell High Energy Synchrotron Source (CHESS), Cornell University, Ithaca, New York 14853, United States

S Supporting Information

ABSTRACT: Dodecanethiol-capped gold (Au) nanocrystal superlattices can undergo a surprisingly diverse series of ordered structure transitions when heated (Goodfellow, B. W.; Rasch, M. R.; Hessel, C. M.; Patel, R. N.; Smilgies, D.-M.; Korgel, B. A. *Nano Lett.* **2013**, *13*, 5710–5714). These are the result of highly uniform changes in nanocrystal size, which subsequently force a spontaneous rearrangement of superlattice structure. Here, we show that halide-containing surfactants play an essential role in these transitions. In the absence of any halide-containing surfactant, superlattices of dodecanethiol-capped (1.9-nm-diameter) Au nanocrystals do not change size until reaching about 190–205 °C, at which point the gold cores coalesce. In the presence of halide-containing surfactant, such as tetraoctylphosphonium bromide (TOPB) or tetraoctylammonium bromide (TOAB), the nanocrystals ripen at much lower temperature and superlattices undergo various ordered structure transitions upon heating. Chloride- and iodide-containing surfactants induce similar behavior, destabilizing the Au–thiol bond and reducing the thermal stability of the nanocrystals.



INTRODUCTION

Dodecanethiol-capped gold (Au) nanocrystals serve as useful models to study superlattice assembly and behavior.^{1–16} Recently, we observed a series of ordered structure changes when superlattices of ~2-nm-diameter dodecanethiol-capped Au nanocrystals were heated.³ As the temperature is increased, the superlattice progresses from an initial body-centered cubic (bcc) arrangement to hexagonal close-packed (hcp), binary simple cubic AB₁₃, and hexagonal AB₅ structure before sintering into bicontinuous gold films at 190 °C. These structural rearrangements result from highly uniform changes in nanocrystal size. Here, we show that the presence of halide-containing surfactant in the superlattice enables particle growth to occur and induces superlattice structure rearrangement at temperatures below the superlattice sintering temperature. Without any halide, the dodecanethiol-capped Au nanocrystals retain their size throughout the heating process until eventually sintering into a bicontinuous gold film.

The dodecanethiol-capped nanocrystals used for these studies are prepared using the Brust–Schiffrin method.¹⁷ The first step of this process involves the transfer of a gold salt from an aqueous solution to an organic solvent using tetraoctylammonium bromide (TOAB) as a phase-transfer catalyst. The gold ions are then displaced from TOAB with dodecanethiol before adding a reducing agent to generate the nanocrystals, and remaining TOAB is removed from the sample during purification of the nanocrystals.^{18–20} Here, we show that residual TOAB in the Au nanocrystal superlattices studied in ref

3 leads to their structure rearrangements upon heating. Superlattices of dodecanethiol-capped Au nanocrystals without any halide present are thermally stable up to about 200 °C. The halides destabilize the Au–thiol bond and promote ligand desorption and nanocrystal growth at reduced temperature. This finding is consistent with the extensive literature examining the role of halides in gold nanocrystal formation and growth that has shown gold nanocrystals to be very sensitive to the presence of halides.^{21–37} Chloride- and iodide-containing surfactants also induce ordered structure rearrangements of 1.9-nm-diameter dodecanethiol-capped Au nanocrystal superlattices when heated.

EXPERIMENTAL DETAILS

Materials. Gold(III) chloride trihydrate (HAuCl₄·3H₂O, >99.9%), tetraoctylammonium bromide (TOAB, 98%), tetraoctylphosphonium bromide (TOPB, 97%), tetraoctylammonium hydrogen sulfate (TOAHS, 97%) 1-dodecanethiol (>98%), sodium borohydride (NaBH₄, >98%), hexadecanol (>99%), dodecylamine (98%), hexadecane (99%), dodecanoic acid (98%), dibenzyl ether (99%), tetrabutylammonium bromide (TBAB, >98%), tetraheptylammonium bromide (THAB, >99%), and tetraoctylammonium chloride (TOAC, >97%) were purchased from Sigma-Aldrich. Toluene (99.9%) was purchased from Fisher. Tetraheptylammonium iodide (THAI, >99%), cetyltrimethylammonium bromide (CTAB, >96%), and cetyltrimethy-

Received: April 24, 2015

Revised: May 22, 2015

Published: May 27, 2015

lammonium chloride (CTAC, >96%) were purchased from Fluka. All chemicals were used as received, and water was doubly distilled and deionized.

Au Nanocrystals. Au nanocrystals were synthesized using a modified Brust-Schiffrin method.^{17,38} In a typical synthesis, 20 mL of an aqueous solution of 328 mg of gold(III) chloride trihydrate ($\text{HAuCl}_4 \cdot 3\text{H}_2\text{O}$, 0.83 mmol) is mixed with 80 mL of toluene and with 6.562 g of tetraoctylammonium bromide (TOAB, 12.0 mmol). This two-phase mixture is stirred for 1 h to complete the phase transfer of AuCl_4^- ions into the organic phase. The organic phase is extracted, and the colorless aqueous phase is discarded. 1-Dodecanethiol (2.5 mmol, 600 μL) is added to the organic phase and stirred for 10 min. Twenty milliliters of an aqueous solution of 378 mg of sodium borohydride (NaBH_4 , 10.0 mmol) prepared in an ice bath is quickly poured into the organic phase while stirring. The two-phase mixture is stirred at 600 rpm for 12 h before the organic phase containing the dodecanethiol-capped Au nanocrystals is extracted.

The nanocrystals are purified by adding 4 mL of ethanol to every 1 mL of crude organic reaction product and then centrifuging at 8500 rpm for 5 min. The supernatant is discarded, and the nanocrystals are redispersed in 3 mL of toluene. This dispersion is centrifuged at 10 000 rpm for 5 min to precipitate poorly capped nanocrystals. The supernatant is collected, and 500 μL of additional 1-dodecanethiol is added to the nanocrystal dispersion. Twenty milliliters of ethanol is added to the nanocrystal dispersion which is then centrifuged at 8000 rpm for 5 min. The supernatant is discarded, and the nanocrystals are redispersed in 3 mL of toluene. Twenty milliliters of ethanol is added to the nanocrystal dispersion again, followed by centrifuging at 8000 rpm for 5 min, discarding the supernatant, and redispersing the nanocrystals with 3 mL of toluene. Twenty milliliters of methanol is added to the nanocrystal dispersion, which is then centrifuged at 8500 rpm for 5 min. The supernatant is discarded and the nanocrystals are redispersed in 3 mL of toluene. This dispersion is centrifuged at 10 000 rpm for 5 min to precipitate poorly capped nanocrystals. The supernatant is retained and dried to determine the mass of the nanocrystals. The nanocrystals are redispersed in toluene at a concentration of approximately 25 mg/mL.

GISAXS. Grazing-incidence small-angle X-ray scattering (GISAXS) was performed on the D1 beamline of the Cornell High Energy Synchrotron Source (CHESS) using monochromatic X-ray radiation of wavelength of 1.154 Å with a bandwidth of ~ 0.017 Å. A fiber-coupled CCD camera (MedOptics) of 1024×1024 pixels with a pixel size of $46.9 \mu\text{m} \times 46.9 \mu\text{m}$ and a 14-bit dynamic range per pixel was used to acquire the GISAXS pattern images, which are dark current-corrected, distortion-corrected, and flat field-corrected by the acquisition software. The sample-to-detector distance was 569.0 mm, determined by using silver behenate powder as a calibration standard. The typical incident angle of the X-ray beam is 0.25° , and the exposure time is around 0.1 to 1 s. GISAXS patterns were background-subtracted, calibrated, and integrated using Fit2D software (version: 12_077_i686_WXP). The GISAXS diffraction spots were indexed using our own software.^{39–41}

GISAXS samples were prepared by drop-casting 20 μL of toluene with Au nanocrystals dispersed at a concentration of 20 mg/mL onto a hand-cut 7 mm \times 7 mm silicon wafer with native oxide placed under a 20 mL vial during drying. Surfactants were added by dispersing 2 mg of Au nanocrystals in 0.1 mL toluene with a dissolved additive (such as TOAB) at 5 mM concentration. This corresponds to a [TOAB]/[thiol] mole ratio of about 1:6. In situ heating of the superlattice is carried out using a copper heating block with the configuration shown in Figure 1, equipped with a heating rod connected to a variac and a thermocouple connected to a temperature controller. GISAXS patterns were acquired every 5 s. Contour plots are generated by radial integration of the 2D scattering intensity. The d spacing related to the scattering features are determined from the 2D scattering vector $q = (q_x^2 + q_z^2)^{1/2}$ where $q = (4\pi/\lambda)\sin(\theta/2)$ (λ is the X-ray wavelength and θ is the scattering angle): $d = \lambda/2 \sin(\theta/2) = 2\pi/q = (2\pi)/((q_x^2 + q_z^2)^{1/2})$.

Transmission SAXS measurements were performed at the University of Texas at Austin using a Molecular Metrology system

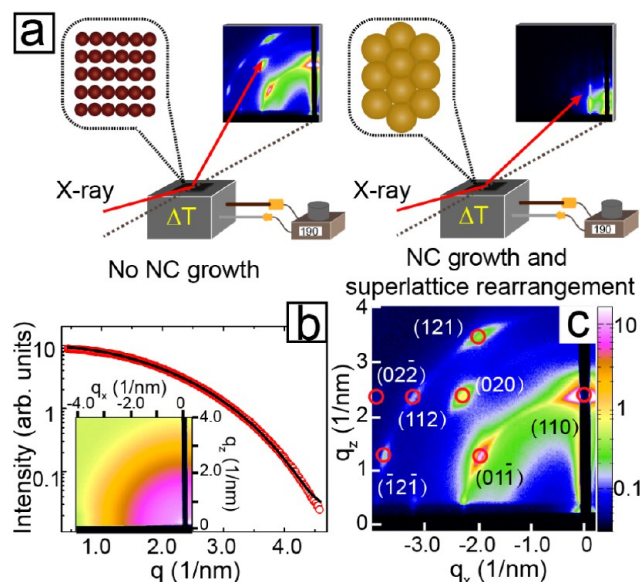


Figure 1. (a) Illustration of the GISAXS system with in situ heating capability. (b) SAXS data (2D scattering pattern shown in the inset) obtained from dodecanethiol-capped Au nanocrystals dispersed in toluene. The best fit of eqs 1–3 to the data (red circles) shown in black gives an average diameter of 1.9 ± 0.19 nm. (c) GISAXS pattern obtained from a superlattice of the nanocrystals measured in (b). The GISAXS pattern indexes to a BCC superlattice with a lattice constant of 3.90 nm, oriented with $(110)_{\text{SL}}$ planes parallel to the substrate.

with a rotating copper anode X-ray source (Bruker Nonius FR591, $\lambda = 0.154$ nm) operating at 3.0 kW and a 2D multiwire gas-filled detector (Molecular Metrology, Inc.). Nanocrystal films were prepared on 1 cm \times 1 cm glass cover slides using the same methods employed for the GISAXS measurements. Solution SAXS data were obtained from nanocrystals dispersed in toluene (5 mg/mL) in a glass capillary tube. All SAXS data have been background subtracted and calibrated.

TEM. Transmission electron microscopy (TEM) was performed on a Tecnai Biotwin TEM operating at a 80 kV acceleration voltage. Samples were prepared by dropping 5 μL of toluene with gold nanocrystals dispersed at a concentration of 2.5 mg/mL onto a carbon-coated copper grid (Electron Microscopy Science, CF200-Cu) held with anticapillary reverse tweezers (Dumont, biology grade) in a 20 mL vial above 2 mL of toluene. TEM images were analyzed using Image-Pro Plus software (Media Cybernetics, Inc.; version 6.0.0.260).

RESULTS AND DISCUSSION

Figure 1 shows SAXS and GISAXS data for dodecanethiol-capped Au nanocrystals used in the study. The SAXS data in Figure 1b were obtained from nanocrystals dispersed in toluene and were used to determine the average size and size distribution of the nanocrystals. Fitting the X-ray scattering intensity $I(q)$ in Figure 1b to a collection of noninteracting nanocrystals of radius R ,⁴²

$$I(q) \propto \int_0^\infty N(R) P(qR) R^6 dR \quad (1)$$

with a shape factor $P(qR)$ for spheres,

$$P(qR) = \left[3 \frac{\sin(qR) - qR \cos(qR)}{(qR)^3} \right]^2 \quad (2)$$

and a Gaussian size distribution $N(R)$,

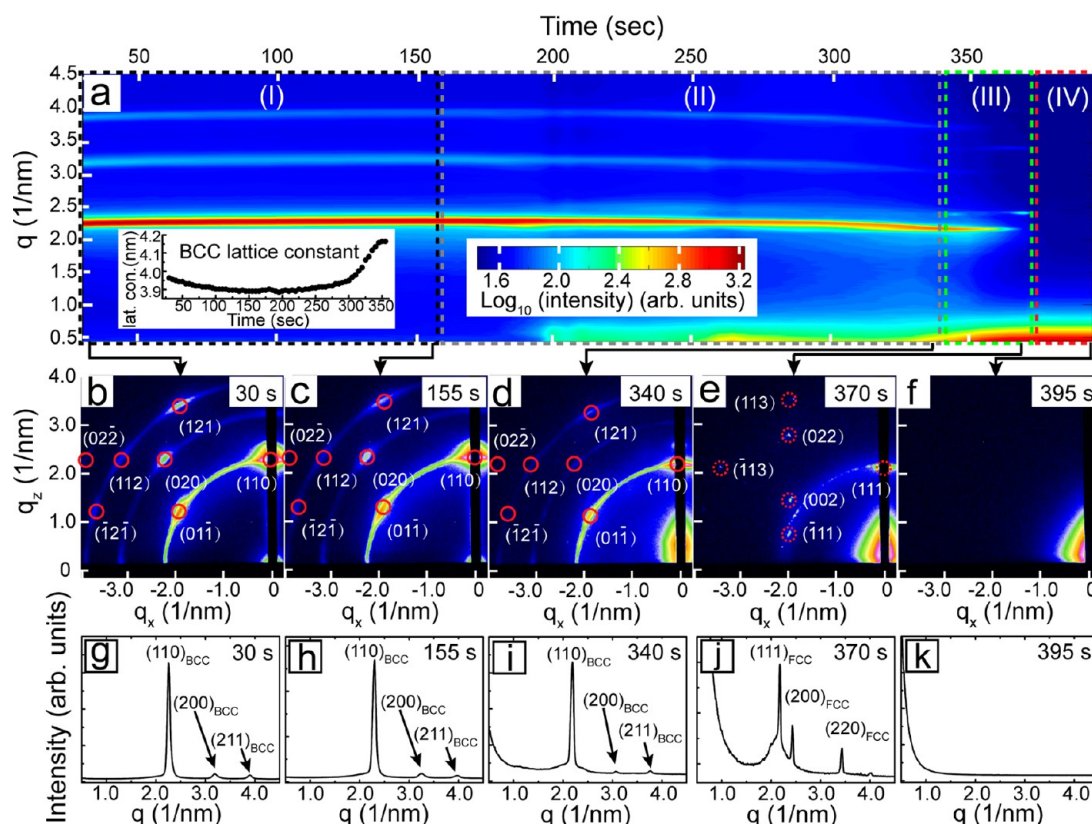


Figure 2. GISAXS data acquired in situ for a superlattice of 1.9-nm diameter dodecanethiol-capped Au nanocrystals heated to 190 °C. The inset shows a plot of the BCC lattice constant against time. (a) Contour plot of the radially integrated scattering intensity versus q as a function of time after reaching 190 °C. (b–f) Full 2D GISAXS patterns of the Au nanocrystal superlattice held at 190 °C for (b) 30 s (BCC structure with $a_{\text{SL}} = 3.96$ nm, oriented with $(110)_{\text{SL}}$ on the substrate), (c) 155 s (BCC structure superlattice with $a_{\text{SL}} = 3.90$ nm, oriented with $(110)_{\text{SL}}$ on the substrate), (d) 340 s (BCC structure with $a_{\text{SL}} = 4.16$ nm, oriented with $(110)_{\text{SL}}$ on the substrate), (e) 370 s (FCC structure with $a_{\text{SL}} = 5.20$ nm, with $(111)_{\text{SL}}$ on the substrate), and (f) 395 s (the superlattice has collapsed). (g–k) Radial integrations of the GISAXS data in (b–f). The red circles in GISAXS patterns are simulated diffraction spots of the superlattices.

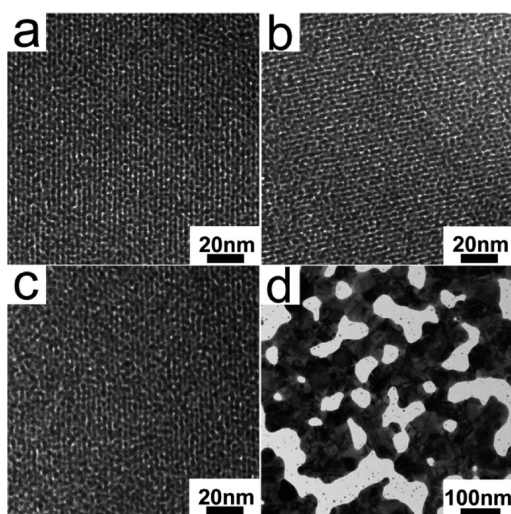


Figure 3. TEM images of 1.9-nm-diameter dodecanethiol-capped Au nanocrystal superlattices (a) prior to heating and after heating at 190 °C for (b) 1 min, (c) 2 min, and (d) 20 min. The superlattices in (a–c) have BCC structure with $(110)_{\text{SL}}$ planes oriented on the substrate. The as-deposited superlattice in (a) has a $(1\bar{1}0)_{\text{SL}}$ d spacing of 2.77 nm, which corresponds to a lattice constant of 3.92 nm that is close to the value of the lattice constant determined from GISAXS. After 20 min of heating, the Au nanocrystals have sintered into a bicontinuous network.

$$N(R) = \frac{1}{\sigma\sqrt{2\pi}} \exp\left[-\frac{(R - \bar{R})^2}{2\sigma^2}\right] \quad (3)$$

gives an average diameter of the Au cores of 1.9 ± 0.19 nm. Figure 1c shows GISAXS data from a collection of nanocrystals deposited on a substrate. The GISAXS pattern exhibits distinct diffraction spots that index to a BCC superlattice with a lattice constant $a_{\text{SL}} = 3.90$ nm and $(110)_{\text{SL}}$ superlattice planes preferentially oriented on the substrate.

Figure 2 shows GISAXS data for the superlattice from Figure 1c after it was heated to 190 °C. The superlattice initially retains its structure, slightly expanding and then contracting ($a_{\text{BCC}}(25\text{ °C}) = 3.90$ nm; $a_{\text{BCC}}(190\text{ °C after 30 s}) = 3.96$ nm; $a_{\text{BCC}}(190\text{ °C after 155 s}) = 3.90$ nm) due to the reorganization of the ligands. A weak scattering feature at low q appears after 340 s, indicating that some of the nanocrystals begin to sinter.^{43–45} The remaining BCC superlattice exhibits a fairly significant lattice expansion at that point ($a_{\text{BCC}}(190\text{ °C after 340 s}) = 4.16$ nm), most likely due to the incorporation of ligands that have desorbed from the sintered regions of the superlattice. The inset in Figure 2a summarizes the change in BCC lattice constant over time. As more sintering occurs, the superlattice continues to expand and eventually undergoes a structural transition to an FCC superlattice. The FCC superlattice structure is oriented preferentially with $(111)_{\text{SL}}$ planes parallel to the substrate with a lattice constant of $a_{\text{FCC}}(190\text{ °C after 370 s}) = 5.20$ nm. This transition is similar to

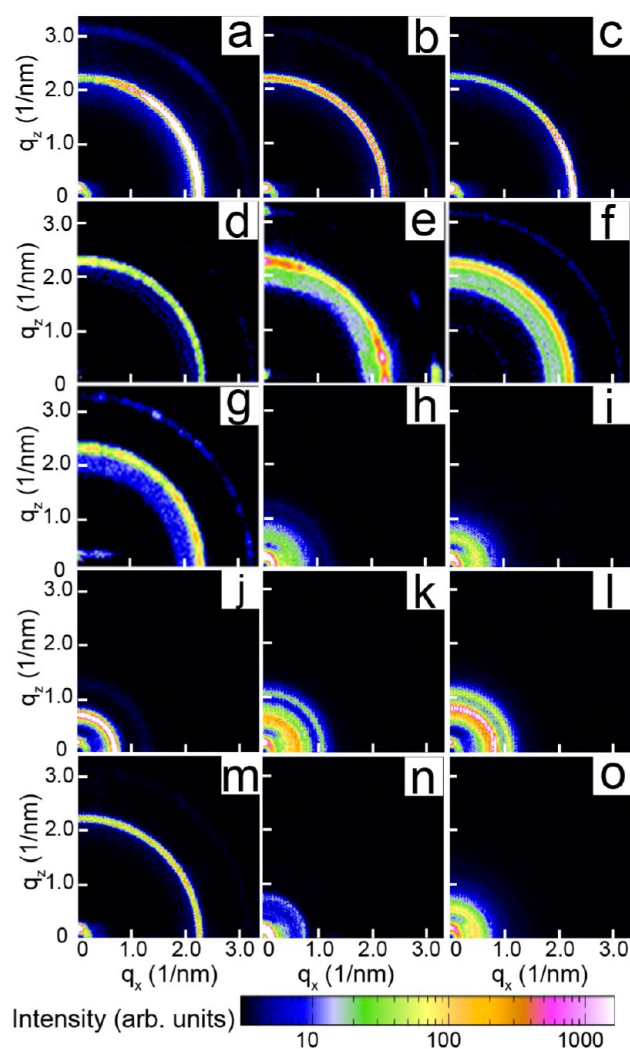


Figure 4. Transmission SAXS of superlattices of 1.9-nm-diameter dodecanethiol-capped Au nanocrystals infiltrated with various additives after being heated at 190 °C: (a) no additive, showing a BCC superlattice with a $(110)_{\text{SL}}$ diffraction ring at 2.25 nm^{-1} and a $(200)_{\text{SL}}$ ring at 3.1 nm^{-1} , (b) 1-dodecanethiol, (c) hexadecanol, (d) dodecylamine, (e) hexadecane, (f) dodecanoic acid, (g) dibenzyl ether, (h) tetrabutylammonium bromide, (i) tetraheptylammonium bromide, (j) tetraoctadecylammonium bromide, (k) tetraoctylammonium chloride, (l) tetraheptylammonium iodide, (m) tetraoctylammonium hydrogen sulfate, (n) cetyltrimethylammonium chloride, (o) cetyltrimethylammonium bromide. The [additive]/[thiol] ratio is about 1:6.

the BCC to FCC superlattice transitions observed in PbSe and PbS superlattices swollen with solvent vapor.⁴⁶ Finally, after 395 s at 190 °C, all of the Au nanocrystals have sintered and there is no longer any evidence of a superlattice structure.

TEM images of the Au nanocrystal assemblies are also consistent with the structure changes observed by GISAXS. Figure 3 shows TEM images of the Au nanocrystal superlattices that were imaged after being heated to 190 °C for 60 s, 120 s, or 20 min. The BCC superlattice structure is stable for the first couple of minutes, and then the nanocrystals sinter. There is no significant change in Au core size prior to sintering.

Figure 4 shows SAXS data for superlattices of 1.9-nm-diameter dodecanethiol-capped Au nanocrystals formed with the addition of various additives after being heated to 190 °C

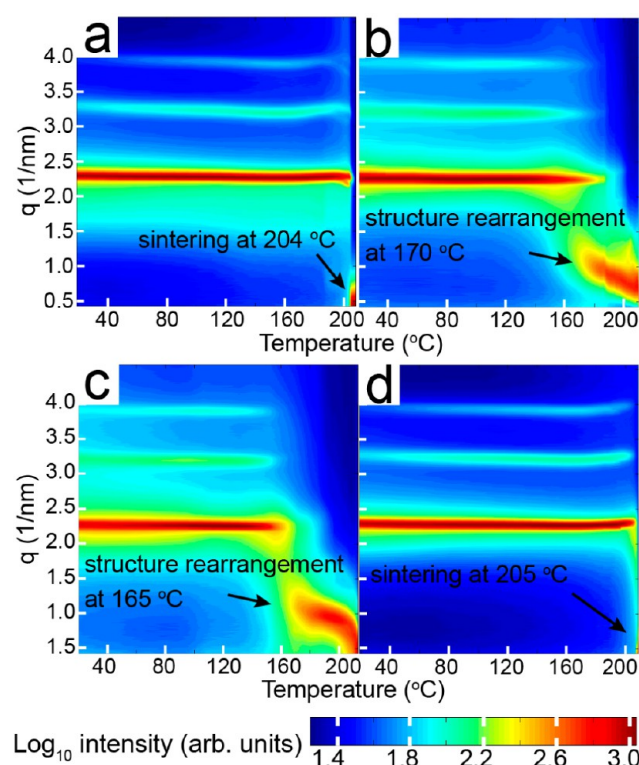


Figure 5. Contour plots of the radially integrated scattering intensity as a function of scattering vector q and temperature during heating the nanocrystal superlattice of (a) 1.9-nm-diameter dodecanethiol-capped Au nanocrystals without additives, showing sintering at 204 °C, and 1.9-nm-diameter dodecanethiol-capped Au nanocrystals with various added surfactants; (b) TOAB, showing structural rearrangement at 170 °C; (c) TOPB, showing structural rearrangement at 165 °C; and (d) TOAHS, showing sintering at 205 °C. The ratio of added surfactant to thiol was 1:6 in all cases.

for 3 min. The superlattice without any additive exhibited the BCC structure described above—a BCC superlattice with a lattice constant of 3.95 nm and no significant change in nanocrystal size or superlattice structure. Similarly, no change in nanocrystal size was observed when the superlattices were infiltrated with excess 1-dodecanethiol (Figure 4b), hexadecanol (Figure 4c), dodecylamine (Figure 4d), hexadecane (Figure 4e), dodecanoic acid (Figure 4f), dibenzyl ether (Figure 4g), or TOAHS (Figure 4m). However, superlattices infiltrated with TBAB (Figure 4h), THAB (Figure 4i), TOAB (Figure 4j), TOAC (Figure 4k), THAI (Figure 4l), CTAC (Figure 4n), and CTAB (Figure 4o) all showed significant changes after heating to 190 °C. Thiols, alcohols, amines, hydrocarbons, carboxylic acids, ethers, and alkyl sulfate salts did not affect the thermal stability of the dodecanethiol-capped Au nanocrystals. Halide ions, i.e., Cl^- , Br^- , and I^- , significantly destabilized the nanocrystals and made them prone to thermally induced ripening.

Figure 5 shows in situ GISAXS data of Au nanocrystal superlattices with added TOAB, TOPB, and TOAHS heated from room temperature to 205 °C. Superlattices without any additives (Figure 5a) and with TOAHS (Figure 5d) showed no significant change in structure until sintering at 204–205 °C, whereas the addition of TOAB (Figure 5b) and TOPB (Figure 5c) induced structural rearrangements at much reduced temperatures of 170 and 165 °C, respectively. The halide ions significantly reduce the thermal stability of the nanocryst-

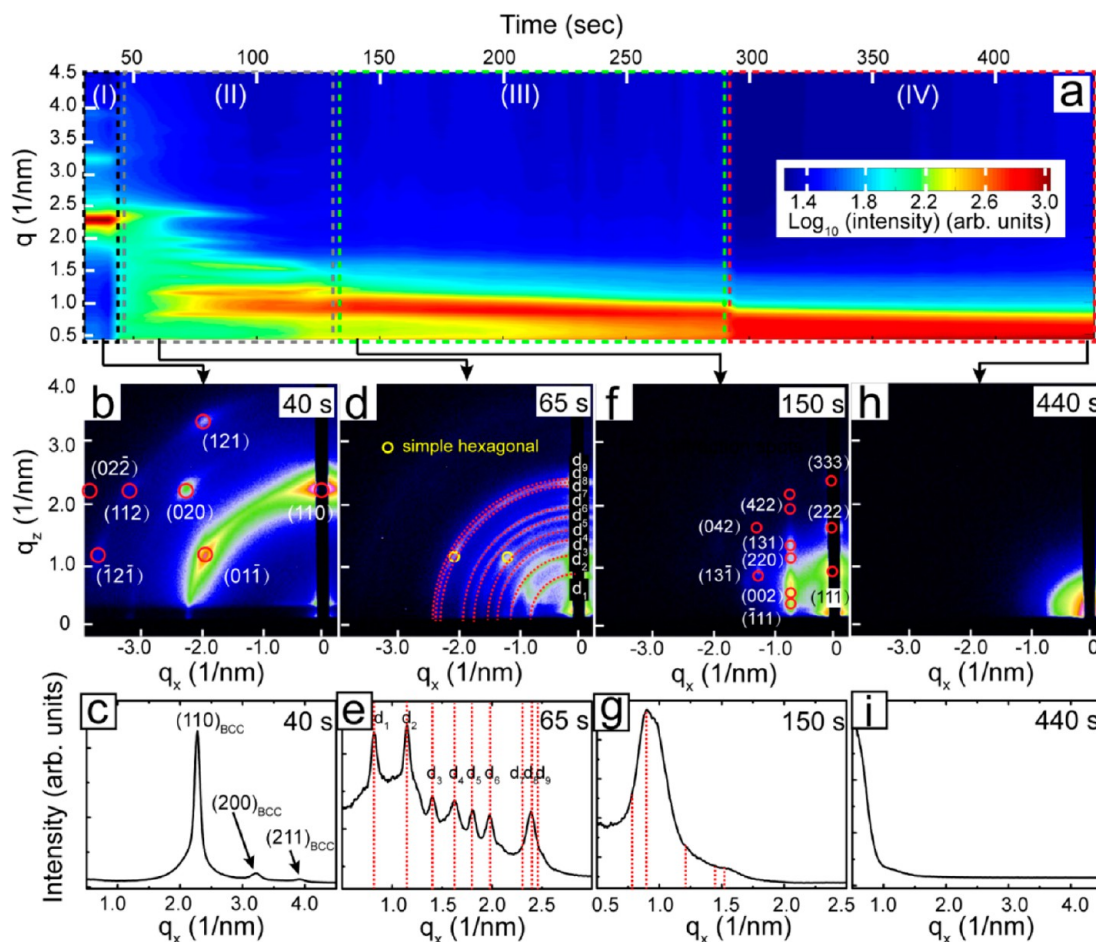


Figure 6. In situ GISAXS data obtained from a superlattice of 1.9-nm-diameter dodecanethiol-capped Au nanocrystals formed with the addition of TOPB ([TOPB]:[thiol] = 1:6) heated to 190 °C. (a) Contour plot of the radially integrated scattering intensity as a function of scattering vector q and time (30–450 s) during in situ GISAXS measurement of the nanocrystal superlattice at 190 °C. (b) GISAXS pattern of the nanocrystal superlattice being heated at 190 °C for 40 s, indexed to a BCC superlattice with a lattice constant of 3.96 nm, oriented with its (110)_{SL} plane parallel to the substrate. (c) Radial integration of the GISAXS pattern in (b), showing (110)_{SL}, (200)_{SL}, and (211)_{SL} diffraction peaks for the BCC superlattice. (d) GISAXS pattern of the nanocrystal superlattice being heated at 190 °C for 65 s, indexed to an ico-AB₁₃ BSL, with a lattice constant of 15.6 nm. The yellow circles highlight the diffraction spots indexed to a simple hexagonal structure. (e) Radial integration of the GISAXS pattern in (d), in which red dashed lines labeled d_1 to d_9 are indexed to (200)_{BSL}, (220)_{BSL}, (222)_{BSL}, (400)_{BSL}, (420)_{BSL}, (422)_{BSL}, (440)_{BSL}, (531)_{BSL}, and (600)_{BSL} diffraction peaks of an ico-AB₁₃ BSL ($a_{\text{ico-AB}_{13}}$ (190 °C after 65 s) = 15.6 nm). (f) GISAXS pattern of the nanocrystal superlattice being heated at 190 °C for 150 s, indexed to an FCC superlattice with a lattice constant of 14.2 nm, oriented with its (111)_{SL} plane parallel to the substrate. (g) Radial integration of the GISAXS pattern in (f), in which red dashed lines highlight the expected diffraction peaks of an FCC superlattice. (h) GISAXS pattern of the nanocrystal superlattice being heated at 190 °C for 440 s, showing no diffraction features. (i) Radial integration of the GISAXS pattern in (h), showing no diffraction features. The red circles in GISAXS patterns are simulated diffraction spots of the superlattices.

als. The minimum amount of TOAB that leads to nanocrystal ripening was about 1 mM or a [TOAB]/[thiol] mole ratio of 1:30 (Figure S9 in Supporting Information).

Figure 6 shows superlattices infiltrated with TOPB examined in finer detail by GISAXS with in situ heating. The superlattice has BCC structure with a slightly larger lattice constant (3.92 nm) than superlattices without added TOPB (3.90 nm). Figure 7a also shows a TEM image of the superlattice prior to heating, which is clearly BCC. Once heated to 190 °C (Figure 6b,c), the BCC structure expands slightly (a_{BCC} (190 °C after 40 s) = 3.96 nm), similar to the superlattice without added TOPB. But after 65 s at 190 °C (Figure 6d,e), the diffraction pattern changes completely from its BCC spot pattern to a series of diffraction rings. This new diffraction pattern indexes to an icosahedral AB₁₃ binary superlattice (ico-AB₁₃ BSL) with a lattice constant of 15.6 nm. One of the distinguishing features of an ico-AB₁₃ BSL is the prominent (531)_{BSL} diffraction peak (labeled as d_8 at

$q = 2.39 \text{ nm}^{-1}$ in Figure 6e).^{47,48} TEM also confirms the ico-AB₁₃ BSL structure (Figure 7c). The ico-AB₁₃ BSL structure is similar to NaZn₁₃ (PDF no. 01-071-9884, space group 226) with simple cubic symmetry and has been widely observed for various nanocrystal assemblies.^{49–51} The appearance of rings in the GISAXS pattern indicates a loss of preferential superlattice orientation on the substrate.

In Figure 6d, there are weak diffraction spots in addition to the strong diffraction rings (yellow circles in Figure 6d). These spots index to a simple hexagonal superlattice with lattice dimensions of $a = b = c = 6.10 \text{ nm}$, $\alpha = \beta = 90^\circ$, $\gamma = 120^\circ$, oriented with (001)_{SL/BSL} planes parallel to the substrate. It is not possible to determine uniquely from the GISAXS pattern if this superlattice structure is a binary superlattice with simple hexagonal structure or a simple hexagonal superlattice. TEM (Figure 7e) showed that the superlattice structure is sh-AB₂ BSL. After 20 s of heating of the TEM sample at 190 °C,

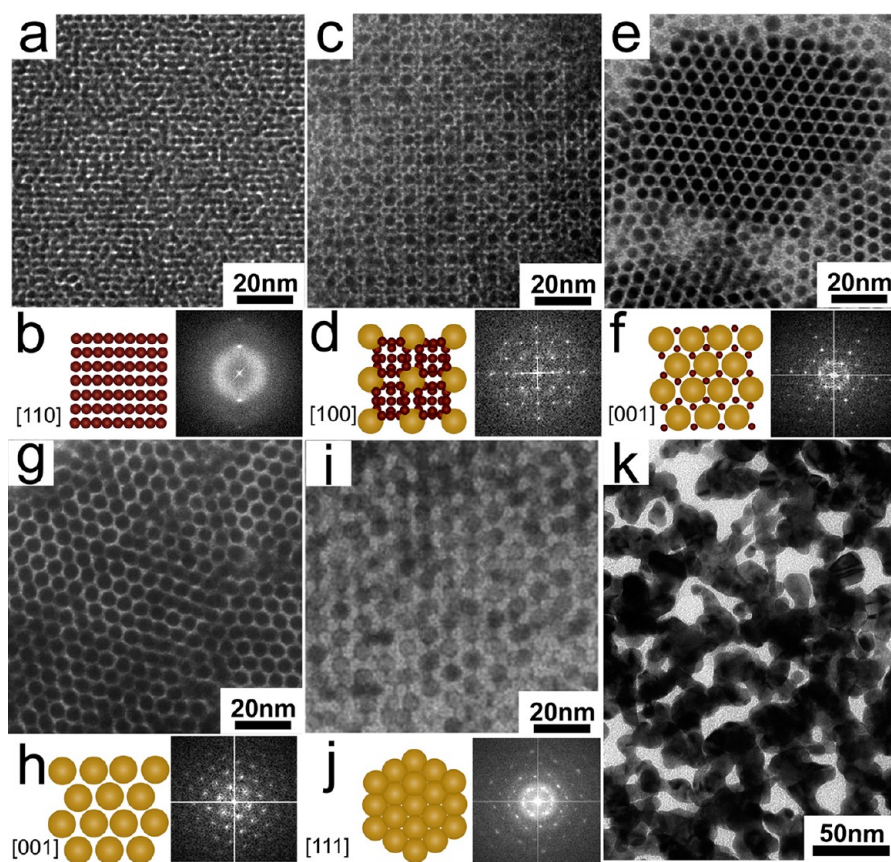


Figure 7. TEM images of nanocrystal superlattices of 1.9-nm-diameter dodecanethiol-capped Au nanocrystals infiltrated with TOPB ([TOPB]:[thiol] = 1:6) heated at 190 °C for various times. (a) 0 s, Au nanocrystals formed the BCC superlattice with lattice constant of 3.95 nm, oriented with its (110)_{SL} plane parallel to the substrate and its [110]_{SL} direction perpendicular to the substrate. (b) Scheme of (110)_{SL} planes of the BCC superlattice and the fast Fourier transform (FFT) of the image in (a). (c) 20 s, Au nanocrystal experienced Ostwald ripening and the superlattice rearranged to an ico-AB₁₃ BSL, oriented with its (100)_{BSL} plane parallel to the substrate and its [100]_{SL} direction perpendicular to the substrate. The (002)_{BSL} *d* spacing of the BSL is 7.32 nm, corresponding to a lattice constant of 14.6 nm. (d) Scheme of (100)_{BSL} planes of ico-AB₁₃ BSL and the FFT of the image in (c). (e) 30 s, the superlattice rearranged to sh-AB₂ BSL, oriented with its (001)_{BSL} plane parallel to the substrate and its [001]_{SL} direction perpendicular to the substrate. The (100)_{BSL} *d* spacing of 4.88 nm corresponds to a lattice constant of $a_{\text{sh-AB}_2}(30 \text{ s}) = 5.64 \text{ nm}$. (f) Scheme of (001)_{BSL} planes of sh-AB₂ BSL and the FFT of the image in (e). (g) 50 s, Au nanocrystals formed a simple hexagonal (SH) superlattice with a lattice constant of 6.36 nm, oriented with its (001)_{SL} plane parallel to the substrate and its [001]_{SL} direction perpendicular to the substrate. (h) Scheme of (001)_{SL} planes of the SH superlattice and the FFT of the image in (g). (i) 50 s, Au nanocrystals also formed an FCC superlattice with a lattice constant of 13.5 nm, oriented with its (111)_{SL} plane parallel to the substrate and its [111]_{SL} direction perpendicular to the substrate. (j) Scheme of (111)_{SL} planes of the FCC superlattice and the FFT of the image in (i). (k) 20 min, Au nanocrystals coalesced to bicontinuous domains of Au.

relatively small regions of simple hexagonal AB₂ BSL (sh-AB₂, isostructure with AlB₂, space group 191) are observed by TEM. After heating for 30 s, the sh-AB₂ BSL becomes the dominant structure as shown in the TEM image in Figure 7e. With further heating, TEM (Figure 7f) showed that the small nanocrystals are ultimately consumed by the larger nanocrystals in the sh-AB₂ superlattice and the structure transforms to a simple hexagonal superlattice with a lattice constant of 6.36 nm.

After 150 s at 190 °C, the GISAXS pattern (Figure 6f,g) continues to evolve and indexes to an FCC superlattice with a lattice constant of 14.2 nm. The spot pattern indicates preferential orientation of the superlattice on the substrate, with (111)_{SL} planes predominantly on the substrate. The FCC structure is also observed by TEM (Figure 7g,h), and the Au core diameter is 5.6 nm. After 440 s at 190 °C, the diffraction pattern finally collapses (Figure 6h,i) as the nanocrystals sinter into the bicontinuous structure shown in the TEM image in Figure 7k.

The structural transitions that occur in the superlattices with added TOPB involve changes in the Au nanocrystal size. In some TEM images, the coexistence of superlattice structures was observed, with a larger lattice mismatch between neighboring domains. The nucleation and growth of the new superlattice domains lead to these grain boundaries.⁵² Figure 8a shows an example of a superlattice phase boundary between a simple hexagonal superlattice region that has nucleated from the edge of a BCC superlattice domain. More TEM images showing the nucleation of the new superlattice structure are provided as Supporting Information. The appearance of the simple hexagonal structure is also unexpected because it has such a low packing density of only 60%—much lower than FCC or HCP (74% packing fraction)—and is not expected to be stable. Figure 8b shows another region of the SH superlattice with three different orientations: the red parallelogram and the green and blue rectangles highlight regions of (001)_{SL}, (100)_{SL}, and (110)_{SL} planes of the SH superlattice, respectively. Only one other case of a simple hexagonal

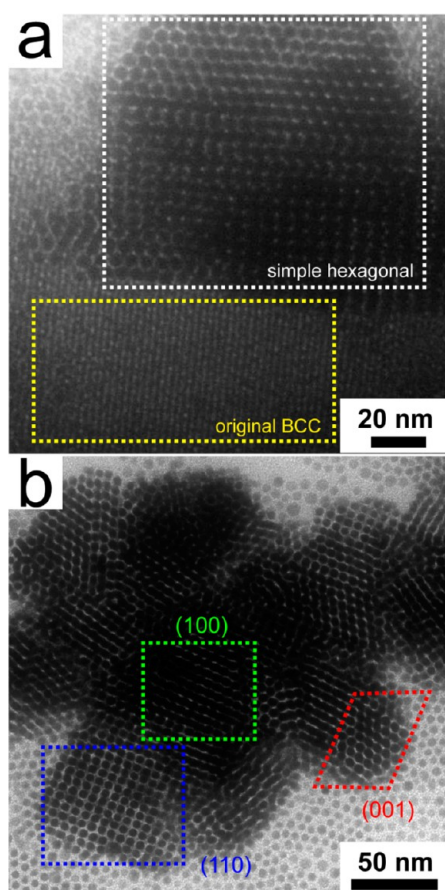


Figure 8. TEM images of a simple hexagonal (SH) superlattice. (a) A domain of the SH superlattice (white rectangle) nucleates from the BCC superlattice matrix (yellow rectangle). (b) BCC superlattice completely rearrange to SH superlattice, in which a red parallelogram highlights the SH superlattice with $(001)_{\text{SL}}$ planes parallel to the substrate, a green rectangle highlights the SH superlattice with $(100)_{\text{SL}}$ planes parallel to the substrate, and a blue rectangle highlights the SH superlattice with $(110)_{\text{SL}}$ planes parallel to the substrate.

superlattice has been observed, also kinetically trapped. In that case, a simple hexagonal sublattice of large Si nanocrystals was retained after small gold nanocrystals had been annealed out of the interstitial sites in a simple hexagonal AB_2 superlattice.⁵³ In this case, the nanocrystals form an SH structure without the use of a template and results from the kinetics of the ripening process.

CONCLUSIONS

The thermal stability of dodecanethiol-capped Au nanocrystals is significantly reduced when halides are present. These results are consistent with other related observations in the literature of halide ions undergoing ligand exchange with thiolates on Au nanocrystal surfaces,^{34,55} promoting Au surface-mediated thiol oxidation, Au nanocrystal ripening in solution,^{21,23} and the induction of the uniform growth of Au nanocrystals in the solid state.^{24,25} Our studies show that with elevated temperature, halides can displace thiolate capping ligands. This thiol displacement is also dependent on the presence of oxygen: both oxygen and halide are required for the heat-induced structure changes that we report here. Because the Au nanocrystals do not ripen in the absence of halides, ligand desorption from the Au nanocrystal surfaces, by a mechanism

of alkanethiol oxidation to alkanesulfonate,²⁸ for example, does not readily occur. And when the gold nanocrystals were heated with added TOAB under an inert atmosphere there was also no significant ripening. We confirmed this essential role of both oxygen and halide by heating a Au nanocrystal film with added TOAB to 190 °C in a nitrogen-filled glovebox and in this case, without any oxygen, there was no evidence of nanocrystal ripening and structural rearrangement (Figure S8 in the Supporting Information). These results show that halide residue remaining from the synthesis incorporated into the Au nanocrystal superlattices underlie the thermally promoted ordered structural rearrangements recently observed by Goodfellow et al.³ in dodecanethiol-capped Au nanocrystals.

We also found that surfactants other than TOAB can induce these structure transitions. The addition of TOPB to Au nanocrystal superlattices, for example, leads to the observed series of ordered structure rearrangements: from BCC to ico- AB_{13} BSL to sh- AB_2 BSL to simple hexagonal or FCC and finally to a sintered structure at elevated temperature. These ordered structural rearrangements also exhibit nucleation and growth similar to atomic solid-state phase transitions. And in some cases, thermodynamically unstable, kinetically trapped, superlattice structures can form, as in the simple hexagonal superlattices observed here.

ASSOCIATED CONTENT

Supporting Information

Experimental setup of GISAXS and TEM sample preparation, details of ico- AB_{13} BSL indexing, TEM images of grain boundaries between different superlattice structures resulting from heat-induced structural rearrangements, TEM images of the random growth of Au nanocrystals in a film not organized into a superlattice, and SAXS data showing the role of oxygen in the observed structure changes and the minimum amount of TOAB needed to reduce the temperature of nanocrystal ripening. The Supporting Information is available free of charge on the ACS Publications website at DOI: 10.1021/acs.langmuir.5b01498.

AUTHOR INFORMATION

Corresponding Author

*E-mail: korgel@che.utexas.edu.

Notes

The authors declare no competing financial interest.

ACKNOWLEDGMENTS

This work was funded by the Robert A. Welch Foundation (grant no. F-1464) and the National Science Foundation (grant no. CBET-140378). CHESS is supported by the NSF and NIH/NIGMS via NSF award DMR-0936384.

REFERENCES

- (1) Andres, R. P.; Bielefeld, J. D.; Henderson, J. I.; Janes, D. B.; Kolagunta, V. R.; Kubiak, C. P.; Mahoney, W. J.; Osifchin, R. G. Self-assembly of a two-dimensional superlattice of molecularly linked metal clusters. *Science* **1996**, *273*, 1690–1693.
- (2) Feldheim, D. L.; Grabar, K. C.; Natan, M. J.; Mallouk, T. E. Electron transfer in self-assembled inorganic polyelectrolyte/metal nanoparticle heterostructures. *J. Am. Chem. Soc.* **1996**, *118*, 7640–7641.
- (3) Goodfellow, B. W.; Rasch, M. R.; Hessel, C. M.; Patel, R. N.; Smilgies, D.-M.; Korgel, B. A. Ordered structure rearrangements in

heated gold nanocrystal superlattices. *Nano Lett.* **2013**, *13*, 5710–5714.

(4) Rasch, M. R.; Rossinyol, E.; Hueso, J. L.; Goodfellow, B. W.; Arbiol, J.; Korgel, B. A. Hydrophobic Gold Nanoparticle Self-Assembly with Phosphatidylcholine Lipid: Membrane-Loaded and Janus Vesicles. *Nano Lett.* **2010**, *10*, 3733–3739.

(5) Whetten, R. L.; Shafgullin, M. N.; Khoury, J. T.; Schaaff, T. G.; Vezmar, I.; Alvarez, M. M.; Wilkinson, A. Crystal structures of molecular gold nanocrystal arrays. *Acc. Chem. Res.* **1999**, *32*, 397–406.

(6) Wu, H.; Feng, B.; Sun, Z.; Haddad, R. E.; Boye, D. M.; Wang, Z.; Fan, H. Pressure-driven assembly of spherical nanoparticles and formation of 1D-nanostructure arrays. *Angew. Chem., Int. Ed.* **2010**, *49*, 8431–8434.

(7) Wu, H.; Bai, F.; Sun, Z.; Hadda, R. E.; Boye, D. M.; Wang, Z.; Huang, J. Y.; Fan, H. Nanostructured gold architectures formed through high pressure-driven sintering of spherical nanoparticle arrays. *J. Am. Chem. Soc.* **2010**, *132*, 12826–12828.

(8) Korgel, B. A.; Fitzmaurice, D. Condensation of ordered nanocrystal thin films. *Phys. Rev. Lett.* **1998**, *80*, 3531–3534.

(9) Sigman, M. B.; Saunders, A. E.; Korgel, B. A. Metal Nanocrystal Superlattice Nucleation and Growth. *Langmuir* **2004**, *20*, 978–983.

(10) Stowell, C.; Korgel, B. A. Self-Assembled Honeycomb Networks of Gold Nanocrystals. *Nano Lett.* **2001**, *1*, 595–600.

(11) Kiely, C. J.; Fink, J.; Brust, M.; Bethell, D.; Schiffrin, D. J. Spontaneous Ordering of Bimodal Ensembles of Nanoscopic Gold Clusters. *Nature* **1998**, *396*, 444–446.

(12) Ohara, P. C.; Leff, D. V.; Heath, J. R.; Gelbart, W. M. Crystallization of Opals from Polydisperse Nanoparticles. *Phys. Rev. Lett.* **1995**, *75*, 3466–3469.

(13) Pileni, M. P. Supracrystals of inorganic nanocrystals: An open challenge for new physical properties. *Acc. Chem. Res.* **2008**, *41*, 1799–1809.

(14) Luedtke, W. D.; Landman, U. Structure, Dynamics, and thermodynamics of passivated gold nanocrystallites and their assemblies. *J. Phys. Chem.* **1996**, *100*, 13323–13329.

(15) Bigioni, T. P.; Lin, X.-M.; Nguyen, T. T.; Corwin, E. I.; Witten, T. A.; Jaeger, H. M. Kinetically driven self assembly of highly ordered nanoparticle monolayers. *Nat. Mater.* **2006**, *5*, 265–270.

(16) Lin, X.-M.; Jaeger, H. M.; Sorenson, C. M.; Klabunde, K. J. Formation of Long-Range Ordered Nanocrystal Superlattices on Silicon Nitride Substrates. *J. Phys. Chem. B* **2001**, *105*, 3353–3357.

(17) Brust, M.; Walker, M.; Bethell, D.; Schiffrin, D. J.; Whyman, R. Synthesis of Thiol-Derivatized Gold Nanoparticles in a Two-Phase Liquid-Liquid System. *J. Chem. Soc., Chem. Commun.* **1994**, 801–802.

(18) Isaacs, S. R.; Cutler, E. C.; Park, J.-S.; Lee, T. R.; Shon, Y.-S. Synthesis of tetraoctylammonium-protected gold nanoparticles with improved stability. *Langmuir* **2005**, *21*, 5689–5692.

(19) Saunders, A. E.; Sigman, M. B.; Korgel, B. A. Growth Kinetics and Metastability of Monodisperse Tetraoctylammonium Bromide Capped Gold Nanocrystals. *J. Phys. Chem. B* **2004**, *108*, 193–199.

(20) Zhu, L.; Zhang, C.; Guo, C.; Wang, X.; Sun, P.; Zhou, D.; Chen, W.; Xue, G. New insight into intermediate precursors of Brust-Schiffrin Gold Nanoparticles Synthesis. *J. Phys. Chem. C* **2013**, *117*, 11399–11404.

(21) Dasog, M.; Scott, R. W. J. Understanding the oxidative stability of gold monolayer-protected clusters in the presence of halide ions under ambient conditions. *Langmuir* **2007**, *23*, 3381–3387.

(22) Moon, S. Y.; Tanaka, S.-I.; Sekino, T. Crystal growth of thiol-stabilized gold nanoparticles by heat-induced coalescence. *Nanoscale Res. Lett.* **2010**, *5*, 813–817.

(23) Hou, W.; Dasog, M.; Scott, R. W. J. Probing the relative stability of thiolate- and dithiolate-protected Au monolayer-protected clusters. *Langmuir* **2009**, *25*, 12954–12961.

(24) Teranishi, T.; Hasegawa, S.; Shimizu, T.; Miyake, M. Heat-induced size evolution of gold nanoparticles in the solid state. *Adv. Mater.* **2001**, *12*, 1699–1701.

(25) Shimizu, T.; Teranishi, T.; Hasegawa, S.; Miyake, M. Size evolution of alkanethiol-protected gold nanoparticles by heat treatment in the solid state. *J. Phys. Chem. B* **2003**, *107*, 2719–2724.

(26) Kanehara, M.; Sakurai, J.-I.; Sugimura, S.; Teranishi, T. Room-Temperature Size Evolution of Thiol-Protected Gold Nanoparticles Assisted by Proton Acids and Halogen Anions. *J. Am. Chem. Soc.* **2009**, *131*, 1630–1631.

(27) Rodríguez-Fernández, J.; Pérez-Juste, J.; Mulvaney, P.; Liz-Marzán, L. M. Spatially-Directed Oxidation of Gold Nanoparticles by Au(III)-CTAB Complexes. *J. Phys. Chem. B* **2005**, *109*, 14257–14261.

(28) Goulet, P. J. G.; Leonardi, A.; Lennox, R. B. Oxidation of gold nanoparticles by Au(III) complexes in toluene. *J. Phys. Chem. C* **2012**, *116*, 14096–14102.

(29) Maye, M. M.; Zheng, W.; Leibowitz, F. L.; Ly, N. K.; Zhong, C.-J. Heating-induced evolution of thiolate-encapsulated gold nanoparticles: A strategy for size and shape manipulations. *Langmuir* **2000**, *16*, 490–497.

(30) Ingham, B.; Lim, T. H.; Dotzler, C. J.; Henning, A.; Toney, M. F.; Tilley, R. D. How nanoparticles coalesce: An in situ study of Au nanoparticle aggregation and grain growth. *Chem. Mater.* **2011**, *23*, 3312–3317.

(31) Schaaff, T. G.; Whetten, R. L. Controlled Etching of Au:SR cluster compounds. *J. Phys. Chem. B* **1999**, *103*, 9394–9396.

(32) Pettibone, J. M.; Hudgens, J. W. Gold cluster formation with phosphine ligands: etching as a size-selective synthetic pathway for small clusters? *ACS Nano* **2011**, *5*, 2989–3002.

(33) Qian, H.; Zhu, M.; Lanni, E.; Zhu, Y.; Bier, M. E.; Jin, R. Conversion of polydisperse Au nanoparticles into monodisperse Au₂₅ nanorods and nanospheres. *J. Phys. Chem. Lett.* **2009**, *113*, 17599–17603.

(34) Wilcoxon, J. P.; Provencio, P. Etching and aging effects in nanosize Au clusters investigated using high-resolution size-exclusion chromatography. *J. Phys. Chem. B* **2003**, *107*, 12949–12957.

(35) Brown, L. E.; Hutchison, J. E. Convenient preparation of stable, narrow-dispersity, gold nanocrystals by ligand exchange reactions. *J. Am. Chem. Soc.* **1997**, *119*, 12384–12385.

(36) Smith, D. K.; Miller, N. R.; Korgel, B. A. Iodide in CTAB Prevents Gold Nanorod Formation. *Langmuir* **2009**, *25*, 9218–9524.

(37) Millstone, J. E.; Wei, W.; Jones, M. R.; Yoo, H.; Mirkin, C. A. Iodide ions control seed-mediated growth of anisotropic gold nanoparticles. *Nano Lett.* **2008**, *8*, 2526–2529.

(38) Rasch, M. R.; Yu, Y.; Bosoy, C.; Goodfellow, B. W.; Korgel, B. A. Chloroform-Enhanced Incorporation of Hydrophobic Gold Nanocrystals into Dioleoylphosphatidylcholine (DOPC) Vesicle Membranes. *Langmuir* **2012**, *28*, 12971–12981.

(39) Smilgies, D.-M.; Blasini, D. R. Indexation scheme for oriented molecular thin films studied with grazing-incidence reciprocal-space mapping. *J. Appl. Crystallogr.* **2007**, *40*, 716–718.

(40) Heitsch, A. T.; Patel, R. N.; Goodfellow, B. W.; Smilgies, D.-M.; Korgel, B. A. GISAXS Characterization of Order in Hexagonal Monolayers of FePt Nanocrystals. *J. Phys. Chem. C* **2010**, *114*, 14427–14432.

(41) Smilgies, D.-M.; Heitsch, A. T.; Korgel, B. A. Stacking of Hexagonal Nanocrystal Layers during Langmuir-Blodgett Deposition. *J. Phys. Chem. B* **2012**, *116*, 6017–6026.

(42) Korgel, B. A.; Fullam, S.; Connolly, S.; Fitzmaurice, D. Assembly and Self-Organization of Silver Nanocrystal Superlattices: Ordered “Soft Spheres”. *J. Phys. Chem. B* **1998**, *102*, 8379–8388.

(43) Korgel, B. A.; Zaccheroni, N.; Fitzmaurice, D. Melting Transition” of a Quantum Dot Solid: Collective Interactions Influence the Thermally-Induced Order-Disorder Transition of a Silver Nanocrystal Superlattice. *J. Am. Chem. Soc.* **1999**, *121*, 3533–3534.

(44) Korgel, B. A. Correlated Membrane Fluctuations in Nanocrystal Superlattices. *Phys. Rev. Lett.* **2001**, *86*, 127–130.

(45) Goodfellow, B. W.; Patel, R. N.; Panthani, M. G.; Smilgies, D.-M.; Korgel, B. A. Melting and sintering of a body-centered cubic superlattice of PbSe Nanocrystals followed by small angle X-ray scattering. *J. Phys. Chem. C* **2011**, *115*, 6397–6404.

(46) Bian, K.; Choi, J. J.; Kaushik, A.; Clancy, P.; Smilgies, D.-M.; Hanrath, T. Shape-Anisotropy Driven Symmetry Transformations in Nanocrystal Superlattice Polymorphs. *ACS Nano* **2011**, *5*, 2815–2823.

- (47) Ketelaar, J. A. A. The crystal structure of alloys of zinc with the alkali and alkaline earth metals and of cadmium with potassium. *J. Chem. Phys.* **1937**, *5*, 668.
- (48) Shoemaker, D. P.; Marsh, R. E.; Ewing, F. J.; Pauling, L. Interatomic distances and atomic valences in NaZn_{13} . *Acta Crystallogr.* **1952**, *5*, 637–644.
- (49) Shevchenko, E. V.; Talapin, D. V.; O'Brien, S.; Murray, C. B. Polymorphism in AB_{13} nanoparticle superlattices: an example of semiconductor-metal metamaterials. *J. Am. Chem. Soc.* **2005**, *127*, 8741–8747.
- (50) Shevchenko, E. V.; Talapin, D. V.; Murray, C. B.; O'Brien, S. Structural Characterization of Self-Assembled Multifunctional Binary Nanoparticle Superlattices. *J. Am. Chem. Soc.* **2006**, *128*, 3620–3637.
- (51) Smith, D. K.; Goodfellow, B. W.; Smilgies, D.-M.; Korgel, B. A. Self-assembled simple hexagonal AB_2 binary nanocrystal superlattices: SEM, GISAXS, and defects. *J. Am. Chem. Soc.* **2009**, *131*, 3281–3290.
- (52) Mnyukh, Y. *Fundamentals of Solid-State Phase Transitions, Ferromagnetism and Ferroelectricity*; DirectScientific Press, 2010.
- (53) Yu, Y.; Bosoy, C. A.; Smilgies, D.-M.; Korgel, B. A. Self-Assembly and Thermal Stability of Binary Superlattices of Gold and Silicon Nanocrystals. *J. Phys. Chem. Lett.* **2013**, *4*, 3677–3682.
- (54) Lohse, S. E.; Burrows, N. D.; Scarabelli, L.; Liz-Marzán, L. M.; Murphy, C. J. Anisotropic Noble Metal Nanocrystal Growth: The Role of Halides. *Chem. Mater.* **2014**, *26*, 34–43.
- (55) DuChene, J. S.; Niu, W.; Abendroth, J. M.; Sun, Q.; Zhao, W.; Huo, F.; Wei, W. D. Halide Anions as Shape-Directing Agents for Obtaining High-Quality Anisotropic Gold Nanostructures. *Chem. Mater.* **2013**, *25*, 1392–1399.